fluids

MDPI

Article

Quantitative Assessment of Red Blood Cell Disaggregation in Chronic Lymphocytic Leukemia via Software Image Flow Analysis

Anika Alexandrova-Watanabe [1,2,†], Emilia Abadjieva [1,2,†], Miroslava Ivanova [3], Lidia Gartcheva [4], Ariana Langari [2,3], Margarita Guenova [4], Tihomir Tiankov [1,2], Elena V. Nikolova [1], Sashka Krumova [3] and Svetla Todinova [2,3,*]

[1] Institute of Mechanics, Bulgarian Academy of Sciences, "Acad. G. Bontchev" Str., Bl. 4, 1113 Sofia, Bulgaria; anikaalexandrova@abv.bg (A.A.-W.); abadjieva@gmail.com (E.A.); tiho_bg@abv.bg (T.T.); elena@imbm.bas.bg (E.V.N.)
[2] Center of Competence for Mechatronics and Clean Technologies—MIRACle, "Acad. G. Bontchev" Str., Bl. 4, 1113 Sofia, Bulgaria; arianalangari@abv.bg
[3] Institute of Biophysics and Biomedical Engineering, Bulgarian Academy of Sciences, "Acad. G. Bontchev" Str. 21, 1113 Sofia, Bulgaria; miroslava.ilieva.ivanova@gmail.com (M.I.); sashka.b.krumova@gmail.com (S.K.)
[4] National Specialized Hospital for Active Treating of Hematological Diseases, Zdrave Str. 2, 1756 Sofia, Bulgaria; l.garcheva@hematology.bg (L.G.); m.genova@hematology.bg (M.G.)
* Correspondence: todinova@abv.bg
† These authors contributed equally to this work.

Abstract

Red blood cell (RBC) aggregation and disaggregation are key factors in microcirculatory flow, and their disturbance can lead to alterations in the rheological properties of blood in disorders such as chronic lymphocytic leukemia (CLL). This study aimed to determine the critical shear rate required to fully disaggregate RBC aggregates using samples from healthy individuals, providing a reference point for evaluating pathological changes. Using a microfluidic system and software-image-based flow analysis, RBC disaggregation was assessed by the Aggregation-Area Indicator at a high shear rate (AAI_H) changes and the number of undestroyed aggregates. The defined critical shear rate at 446 s^{-1} was applied to assess RBC disaggregation in CLL patients, both untreated and treated with Obinutuzumab/Venetoclax or Ibrutinib. CLL samples exhibited significantly elevated AAI_H values compared to controls, indicating a greater resistance to shear-induced dispersion. Although both treatments reduced the number of stable aggregates, neither therapy fully normalized RBC disaggregation to the levels observed in healthy controls. Moreover, there was a notable heterogeneity among Ibrutinib-treated patients, revealing different therapeutic effects on RBC rheology. These findings suggest alterations in the RBC rheology in CLL despite therapy and support the use of a shear-dependent disaggregation analysis as a complementary tool for understanding and monitoring CLL-related hematologic abnormalities.

Keywords: red blood cell disaggregation; microfluidic device; software image flow analysis; Obinutuzumab-Venetoclax; Ibrutinib

check for updates

Academic Editor: Laura A. Miller

Received: 30 April 2025
Revised: 10 June 2025
Accepted: 26 June 2025
Published: 27 June 2025

Citation: Alexandrova-Watanabe, A.; Abadjieva, E.; Ivanova, M.; Gartcheva, L.; Langari, A.; Guenova, M.; Tiankov, T.; Nikolova, E.V.; Krumova, S.; Todinova, S. Quantitative Assessment of Red Blood Cell Disaggregation in Chronic Lymphocytic Leukemia via Software Image Flow Analysis. *Fluids* **2025**, *10*, 167. https://doi.org/10.3390/fluids10070167

Copyright: © 2025 by the authors. Licensee MDPI, Basel, Switzerland. This article is an open access article distributed under the terms and conditions of the Creative Commons Attribution (CC BY) license (https://creativecommons.org/licenses/by/4.0/).

1. Introduction

Red blood cells (RBCs), the most abundant type of blood cells, are the primary determinants of rheological blood behavior. Their physical properties influence blood viscosity, flow resistance, and microcirculatory perfusion. The characteristic biconcave shape and

specific membrane protein composition allow them to deform and pass through capillaries smaller than their diameter, maintaining continuous microcirculatory blood flow [1].

At low shear rates (<1–10 s^{-1}), RBCs aggregate due to intercellular adhesion, forming two- and three-dimensional structures. The aggregation results in the formation of rouleaux—piles of RBCs resembling stack of coins. As aggregation intensifies, these linear arrays may develop branches, leading to the emergence of more complex structures. In some cases, interconnected rouleaux form continuous networks that may further assemble into large, three-dimensional aggregates, depending on the intercellular adhesion forces [2]. RBC aggregation is a reversible, dynamic process that increases blood viscosity at low shear rates and plays a key role in regulating microvascular blood flow [3].

The aggregation of RBCs is controlled by a balance between intrinsic factors (cell properties such as deformability, membrane fluidity, and surface charge) and extrinsic factors (including hematocrit and plasma levels of high-molecular-weight proteins). A reduction in cell elasticity and membrane fluidity increases cell adhesion and promotes aggregation, impairing blood flow and increasing vascular resistance [4]. The external factors also have a significant impact on aggregation. Elevated levels of high-molecular-weight proteins (e.g., fibrinogen) or polymers (e.g., Dextran 70 kDa) enhance RBC aggregation by promoting cell–cell interactions [2,5].

As shear rates increase above a critical value, hydrodynamic forces exceed the weak adhesive interactions between aggregated RBCs, leading to their dispersion and, thus, to a decrease in blood viscosity. This process is essential for maintaining hemodynamic stability, particularly in microcirculation [6,7].

Excessive RBC aggregation and impaired RBC disaggregation could disrupt oxygen delivery and promote vascular resistance [8,9]. The dynamics of RBC aggregation and disaggregation are closely linked to cellular deformability and surface characteristics. These properties can be altered by various factors, including cellular aging, oxidative stress, and the activity of proteolytic enzymes, all of which influence the composition and function of the RBC membrane and intercellular interactions. In inflammatory states, elevated levels of chemotactic factors, reactive oxygen species (ROS), and proteolytic enzymes further damage RBCs, reducing their flexibility, promoting aggregation, and hindering proper disaggregation. The ability of RBCs to dynamically transition between aggregation and disaggregation states plays a vital role in modulating blood flow resistance and ensures efficient oxygen delivery throughout the microcirculation. Disruptions in this finely tuned balance, as seen in conditions like hyperviscosity syndromes, diabetes, or chronic inflammatory conditions, can lead to impaired microcirculation and an increased risk of cardiovascular complications [10–12]. Inflammation is thought to be involved in the initiation and progression of several chronic lymphoproliferative disorders of the B-cell type, such as CLL, non-Hodgkin lymphoma, multiple myeloma, etc. [13].

CLL is a type of cancer characterized by the accumulation of abnormal B cells in the blood and bone marrow [14]. The malignant cells often infiltrate the lymph nodes, spleen, and liver, leading to various complications. In CLL, malignant B cells partly escape programmed death by overproducing BCL-2, an anti-apoptotic protein that inhibits the normal process of apoptosis. Another critical mechanism supporting CLL cell survival is the activation of the B-cell receptor (BCR) signaling pathway, which also leads to the increased production of inflammatory cytokines and promotes a microenvironment conducive to leukemic cell persistence [15]. Pro-inflammatory cytokines and chemokines, such as interleukin-6 (IL-6), tumor necrosis factor-alpha (TNF-α), and B-cell activation factor (BAFF), were found to be elevated in CLL patients [16,17]. These inflammatory mediators can affect RBC behavior, potentially leading to altered aggregation dynamics.

Furthermore, CLL is associated with autoimmune complications, including autoimmune hemolytic anemia (AIHA), where the immune system wrongly targets and destroys RBCs [18]. The occurrence of AIHA can further exacerbate disruptions in RBC aggregation as a consequence of their impaired morphology and function [19]. These factors highlight the impact of chronic inflammation in CLL on the aggregation–disaggregation process and microcirculatory dynamics of RBCs.

Several inhibitors targeting the BCL-2 family are developed, among which Venetoclax stands out as a selective BCL-2 inhibitor that effectively induces apoptosis in CLL cells [20].

Another major advancement in CLL therapy is Ibrutinib, a first-in-class Bruton's tyrosine kinase (BTK) inhibitor. It binds irreversibly to a cysteine residue (Cys481) within the active site of BTK, thereby disrupting key signaling pathways that support the proliferation and survival of malignant B cells [21].

In the past decade, advances in microfluidic technologies have significantly enhanced the experimental characterization of RBC properties, as well as the rheological behavior of blood [22]. In this context, microfluidic systems offer a significant advantage since they allow for precise fluid flow control, enabling a detailed examination of RBC deformability, aggregation, and disaggregation under various conditions. These emerging technologies provide valuable insights into the effect of the mechanical properties of RBCs on blood viscosity, microcirculatory flow, and overall hemodynamics. In particular, microfluidic systems enable the study of pathological conditions, such as sickle cell disease, diabetes, CLL, and other disorders, in which altered RBC behavior contributes to impaired oxygen delivery and increased vascular resistance [9,23–25].

Recently, we developed a Software Image Flow Analysis platform to differentiate the effects of various targeted therapies on the aggregation behavior of RBCs in CLL [25]. We found that RBC aggregation was significantly higher in untreated CLL patients than in healthy controls. Targeted therapy with a combination of Obinutuzumab and Venetoclax did not lead to an improvement in RBC aggregation compared to untreated CLL patients, which suggests that the therapy does not directly modulate the processes contributing to an altered RBC rheology. In contrast, the treatment with Ibrutinib restored the RBC aggregation levels to those observed in healthy individuals. This indicates that Ibrutinib may exert beneficial effects not only on malignant lymphocytes but also on blood rheology. The likely mechanism involves its immunomodulatory activity, which reduces chronic inflammation and circulating cytokine levels—factors known to affect RBC membrane properties and promote aggregation.

In this study, we further extend our investigation by examining the critical shear rate required for effective RBC disaggregation in healthy individuals and assess its clinical relevance in CLL patients. Using a microfluidic software-image-based flow analysis platform, we aim to quantitatively evaluate RBC aggregation dynamics, identify potential alterations in key rheological parameters associated with CLL, and evaluate the response of the applied therapies. Our results revealed impaired RBC disaggregation in the samples of untreated CLL patients, and a partially reduced number of aggregates in Obinutuzumab/Venetoclax- and Ibrutinib-treated patients. Moreover, Ibrutinib-treated patients displayed high inter-individual variability in the rheological response.

2. Materials and Methods

2.1. Study Groups and Ethics Statement

This study enrolled a total of 27 patients with CLL who were admitted to the National Specialized Hospital for Active Treatment of Hematological Diseases, Sofia, Bulgaria. The diagnosis of CLL was established following the current CLL guidelines [26,27]. Exclusion

criteria were as follows: patients with comorbid conditions such as diabetes, renal disease, autoimmune diseases, or hyperlipidemia were excluded from participation.

The study cohort was divided into three groups: 8 untreated patients (3 females, 5 males; mean age: 60.5 ± 12.3 years) with asymptomatic or mild disease; 11 patients undergoing therapy with a combination of Obinutuzumab/Venetoclax (5 females, 6 males; mean age: 69.6 ± 7.5 years); and 8 patients receiving treatment with Ibrutinib (3 females, 5 males; mean age: 64.13 ± 9.2 years).

The control group included 16 healthy volunteers (10 females, 6 males; mean age: 56.4 ± 6.8 years) with no history of chronic or oncohematological diseases and who are free of medication at the time of enrollment.

All patients and healthy subjects gave their written informed consent for participation. The study protocol was approved by the Ethics Committee of the Institute of Biophysics and Biomedical Engineering, Bulgarian Academy of Sciences (Approval No. 378НД 26 March 2024), and conducted following the Declaration of Helsinki.

2.2. Blood Collection and Sample Preparation

Peripheral blood samples were obtained from CLL patients following an overnight fast, coinciding with their routine hospital visits. Venous blood was drawn into two 6 mL Vacutainer tubes containing K_2EDTA (Becton Dickinson and Company, Franklin Lakes, NJ, USA). RBCs were subsequently isolated following the methodology outlined by Alexandrova-Watanabe et al. [24]. In brief, following centrifugation of the collected blood (Universal 320 R centrifuge, Hettich, Germany) at 1500 *g* for 10 min, the supernatant, comprising plasma and white blood cells, was carefully removed. The remaining RBCs were resuspended and washed twice with phosphate-buffered saline (140 mM NaCl, 2.7 mM KCl, 8 mM Na_2HPO_4, 1 mM KH_2PO_4). The final RBC suspension was adjusted to a hematocrit of 40% (by centrifuge Haematokrit 200, Hettich, Germany).

2.3. Stimulation of RBC Aggregation

In order to induce RBC aggregation with comparable strength and kinetics to that caused by plasma proteins such as fibrinogen, while avoiding the variability of patient plasma [28,29], 5 µL of RBCs from each blood sample, obtained from healthy controls and CLL patients, were mixed with 195 µL of Dextran 70 solution (4 g/dL). The chosen Dextran concentration offers a balance between physiologically relevant aggregation and low solution viscosity, providing a standardized model for comparing healthy and pathological RBC samples [30]. This dilution reduced the final hematocrit of the RBC suspension to 2% across all experiments.

2.4. Viscosity Measurements

The viscosity of RBC suspensions diluted in Dextran 70 (as described in Section 2.3) was measured under steady-state flow conditions employing a Brookfield programmable rotational viscometer type DV-II + Pro (Brookfield Engineering Laboratories, Inc., Middleboro, MA, USA). Before measurements, the viscometer was calibrated using water at a temperature of 37 °C to ensure accuracy. At the same temperature, the viscosity of the diluted RBC suspensions was determined to be 1.12 ± 0.04 mPa.s.

2.5. Microfluidic System Description and Experiments

An air-pressure-driven BioFlux microfluidic system (Cell Microsystems, Durham, NC, USA) was employed to study RBC aggregation under flow conditions [25]. This system provides a high-resolution imaging platform optimized for in-flow rheological analyses. It includes the BioFlux 200 electro-pneumatic flow control pump, a Lumascope 620 inverted fluorescence microscope, Lumascope 620 (Etaluma, San Diego, CA, USA), BioFlux

microfluidic plates, and a computer workstation equipped with Lumaview software (Version: 19.07.12) for system control and data acquisition.

The RBC aggregation assays were conducted in BioFlux 24-well plates configured for 0–20 dyn/cm^2 shear stress. Each plate contained eight microfluidic channels with a cross-sectional width of 350 μm and a height of 75 μm [25].

2.6. Design of the Aggregation Experiments

Microfluidic channels were loaded with 200 μL of each diluted RBC suspension prepared in Dextran 70. To eliminate pre-existing RBC aggregates, the suspensions were initially perfused through the channels at a high shear stress of 5 dyn/cm^2 (corresponding to a shear rate of 446 s^{-1}) for 5 min. Following this, the flow was abruptly reduced to a low shear stress of 0.1 dyn/cm^2 (shear rate of 8.9 s^{-1}) for an additional 5 min to promote aggregation under low-flow conditions.

Subsequently, flow was completely halted, and RBC aggregates were visualized using an inverted phase-contrast microscope. Image acquisition began 30 s after flow cessation, with at least five images captured every 2 s along the full visible length of the channel at randomly selected locations.

The 2D images presented in this study are extracted from a cross-section of the microchannel, captured near the bottom surface (i.e., the bottom wall of the microchannel). Thus, the phase-contrast microscopy is focused near the bottom of the microchannel. Therefore, the horizontal axis (x-axis) represents the position along the length of the microchannel (i.e., the direction of flow), while the vertical axis (y-axis) corresponds to the distance perpendicular to the microchannel floor. Furthermore, the visualized plane in the images does not show the full height of the microchannel, but only a thin optical section near the microchannel wall. This allows for detailed observation of cell–cell and cell–surface interactions, which are relevant for analyzing the dynamics of aggregation under flow.

2.7. Design of the Disaggregation Experiments

For the experiment aimed at determining the critical shear rate, RBC aggregates formed in suspensions from healthy individuals were exposed to increasing shear stresses of 1, 2, 3, 4, 5, and 6 dyn/cm^2, corresponding to shear rates of 89, 178, 268, 357, 446, and 535 s^{-1}, respectively. The critical shear stress was defined as the minimum shear stress at which complete disaggregation was observed. This parameter was determined in samples from untreated CLL patients and subsequently applied in experiments assessing the degree of RBC disaggregation after the applied targeted treatments.

After each applied shear rate (maintained for 5 min), undestroyed RBC aggregates—i.e., those not disaggregated by the applied flow—were visualized using phase-contrast microscopy. Image acquisition began 30 s after the cessation of flow, with at least five images captured every 2 s along the entire visible length of the microfluidic channel. Fields of view were randomly selected to ensure representative sampling.

2.8. Computational Image Analysis for Red Blood Cell Aggregate Classification and Visualization

For this study, based on the developed computational approach [25] to analyze and quantify RBC aggregates, a custom macro software application (Software Image Flow Analysis platform) within the Image J 1.54g [https://imagej.net/ij/, accessed on 11 November 2024] environment was implemented. This software application, constructed using Image J's scripting capabilities, executes a methodical procedure to evaluate and visually represent RBC aggregates according to their size characteristics. The Software Image Flow Analysis (workflow) proceeds through multiple distinct stages.

Initially, the system imports image data into the Image J 1.54g platform. The images are further processed to prepare them for accurate analysis. This preparation involves

binary conversion utilizing Image J's thresholding functionalities, distinguishing RBC aggregates from the background. After thresholding, additional programming steps are applied to ensure that each RBC aggregate is processed as a cohesive region, preserving the structural integrity necessary for accurate quantitative analysis.

For the next stage, the analytical parameters (the area and number of RBC aggregates) are chosen, with particular emphasis on dimensional quantification. The classification criterion is the surface area, expressed in square micrometers (μm^2). This metric is calculated by quantifying the pixel composition of each aggregate through the area parameter within the Set Measurements function of Image J, and the result is then converted into real-world size (μm^2) based on the image's scale.

The next functional step is the realization of the quantitative evaluation that includes the Analyze Particles functionality of Image J to determine RBC aggregates with specific criteria:

- Identifying RBC aggregates with dimensional parameters exceeding 50 μm^2 with no defined upper limit;
- Systematic cataloging within the Region of Interest (ROI) Manager of Image J for further analysis processing.

Visual differentiation is accomplished through a dimensional classification scheme with the corresponding color designation (Table 1).

Table 1. Classification of RBC aggregates by size and color mapping.

Area Range (μm^2)	Color
<99	White
100–330	Green
331–660	Blue
661–1320	Light Blue
1321–2700	Purple
>2701	Yellow

Each identified RBC aggregate undergoes individual analysis involving ROI Manager selection, dimensional assessment, and appropriate color application through visualization functions. Each identified RBC aggregate is visualized by delineating its perimeter with a colored outline. The color of each outline corresponds to the aggregate's size classification, creating a clear visual representation of the size distribution within the image. A standardized line ensures optimal border visibility for all RBC aggregated structures.

This final step indicates the completion of the analytical process, with all aggregates classified, color-coded, and quantified according to their respective size categories (i.e., the number of RBC aggregates and the total area of RBC aggregates at each defined colored size interval).

2.9. RBC Aggregation Indices

Two primary parameters were used to quantify RBC aggregation through image analysis: the RBC Aggregate-Area Indicator (AAI) and the Number of RBC Aggregates (NA), both assessed under low (L)- and high (H)-shear-rate conditions (denoted as subscripts).

The NA parameter was defined as the average number of distinct RBC aggregates per unit area of the microscope's visual field. AAI quantifies the extent of RBC aggregation by comparing the area covered by RBC aggregates to the total area of the visual field of the microscope. AAI_L represents the degree of RBC aggregation under low-flow conditions and is calculated by the following formula [adapted from 3]:

$$AAI_L = \frac{S_2}{S_1}, \quad (1)$$

where S_2 (in pixels) is the total sum of areas of the aggregates after the flow of 8.9 s^{-1}, and S_1 (in pixels^2) is the total observed area of one visual field of the microscope. AAI_H presents undispersed RBC aggregates at high-flow conditions, which are calculated by the formula:

$$AAI_H = \frac{S_3}{S_1}, \quad (2)$$

where S_1 (in pixels) is the total observed area of one visual field of the microscope (1600 × 300 pixels^2), and S_3 (in pixels) is the total sum of areas of RBC aggregates which were not disaggregated at high shear rate.

2.10. Clinical and Hematological Indices

The clinical and hematological indices were obtained from the National Specialized Hospital for Active Treatment of Hematological Diseases, Sofia, Bulgaria. Biochemical analyses were performed using the Architect c4000 and Beckman Coulter AU480 analyzers (Chaska, MN, USA). Hematological analyses were conducted with the Siemens ADVIA 2120i (Tarrytown, New York, USA) and Dirui BF-7200 Plus systems (Dirui Industrial Co., Ltd., Changchun, China). Fibrinogen levels were assessed using the Sysmex CS-2500 coagulation analyzer (Sysmex Corporation, Kobe, Hyōgo Prefecture, Japan). All procedures were carried out in accordance with standard clinical protocols.

2.11. Theoretical Assumptions on Flow Field, Shear Rate Distribution, and Shear-Induced RBC Migration in the Context of BioFlux Experimental Analysis

Given the dilute nature of the erythrocyte suspension (2% hematocrit in 4 g/dL Dextran 70), it exhibits a nearly constant viscosity (1.12 ± 0.04 mPa.s at 37 °C), supporting the assumption that it behaves approximately as a Newtonian fluid. Under this assumption, the velocity profile along the channel height is almost parabolic, and the shear rate varies linearly, ranging from zero at the centerline to a maximum at the walls. A schematic illustration of the expected velocity and shear rate profiles is provided in Figure 1. This spatial variation in shear rate is critical for understanding aggregation dynamics. Even at relatively high nominal wall shear stress (e.g., 5 dyn/cm^2), regions of low shear rate remain near the channel centerline. These zones allow for the partial retention of aggregates (rouleaux), as the shear forces present may be insufficient for complete disintegration, a phenomenon previously reported in similar microfluidic studies [31].

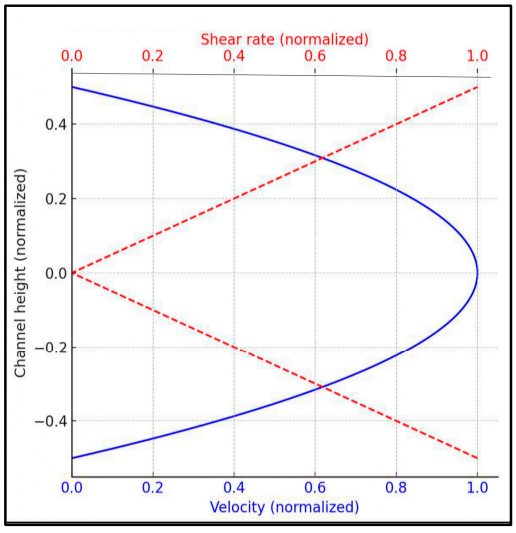


Figure 1. Velocity and shear rate profiles in a rectangular microchannel (Newtonian fluid).

The analytical expressions used in this study to estimate the nominal and local shear rates in the microfluidic system are presented below.

2.11.1. Nominal Shear Rate

Due to the non-uniform shear rate profile in rectangular microchannels, the shear rates reported in this study refer to nominal values, calculated based on the geometry of the channel and the imposed flow conditions. Specifically, the nominal shear rate $\dot{\gamma}_{nom}$ is approximated by the following formula [32]:

$$\dot{\gamma}_{nom} = \frac{6Q}{wh^2} \tag{3}$$

where Q is the volumetric flow rate, w is the channel width, and h is the channel height.

The BioFlux 200 software to V2.6.0.9 directly calculates it at a given nominal shear stress value $\tau_{nom} = \dot{\gamma}_{nom}$, where the value of the effective dynamic viscosity μ is experimentally determined for the studied RBC suspension (see Section 2.4). The volumetric flow rate Q is indirectly determined by the applied pressure differential (ΔP) set by the BioFlux control software and is internally calibrated for the channel geometry. It is obvious that the nominal shear rate defined by Equation (3) coincides with the maximal shear rate, and it provides a standardized comparative metric for aggregation/disaggregation across experiments.

2.11.2. A Local Shear Rate Approximation

The BioFlux system does not provide direct access to spatially resolved flow fields or shear rate profiles. Thus, building upon the nominal shear rate defined above, we now present a physically grounded approximation for the local shear rate within the microchannel, which more accurately reflects the shear conditions in the studied RBC suspension flow. This local shear rate will be used throughout the subsequent analysis of the study.

Because the velocity profile u(y) across the channel height $y \in \left[-\frac{h}{2}, \frac{h}{2}\right]$, is parabolic; it can be expressed as follows:

$$u(y) = \frac{3}{2}\overline{u}\left(1 - \left(\frac{2y}{h}\right)^2\right) \tag{4}$$

where $\overline{u} = \frac{Q}{wh}$ is the mean flow velocity.

The local shear rate (velocity gradient) is the spatial derivative of velocity:

$$\dot{\gamma}(y) = \left|\frac{du}{dy}\right| = \frac{12\overline{u}}{h^2}|y| \tag{5}$$

The maximum shear rate occurs at the channel walls $y = \pm\frac{h}{2}$

$$\dot{\gamma}_{max} = \dot{\gamma}\left(\pm\frac{h}{2}\right) = \frac{6Q}{wh^2} = \dot{\gamma}_{nom} \tag{6}$$

To obtain the average local shear rate experienced by particles or cells distributed over the channel height, we take the spatial average of $\dot{y}(y)$:

$$\dot{\gamma}_{local} = \frac{1}{h}\int_{-\frac{h}{2}}^{\frac{h}{2}} \dot{\gamma}(y)dy = \frac{1}{h}\int_{-\frac{h}{2}}^{\frac{h}{2}} \frac{12\overline{u}}{h^2}|\gamma|d\gamma = \frac{3\overline{u}}{h} \tag{7}$$

Using $\overline{u} = \frac{Q}{wh}$, this simplifies to the following:

$$\dot{\gamma}_{local} = \frac{3Q}{2wh^2} = \frac{1}{2}\dot{\gamma}_{nom} \tag{8}$$

This result shows that the average local shear rate in the channel cross-section is approximately half of the nominal (maximum) shear rate defined at the walls. Physically, this indicates that the RBC suspension experiences a range of shear rates, from zero at the center to the maximum shear rate $\dot{\gamma}_{nom}$ at the microchannel wall. The average shear rate is approximately half the maximum. Therefore, using $\dot{\gamma}_{local} \approx \frac{1}{2}\dot{\gamma}_{nom}$ is a physically sound and practical approximation for microfluidic experiments involving near-Newtonian fluids.

2.11.3. Shear-Induced Migration in the Context of Dilute RBC Suspensions

Although the present study did not explicitly investigate shear-induced migration of RBCs, it is worth noting that such migration can occur even under the present experimental conditions involving a dilute RBC suspension (2% hematocrit) in a Newtonian medium (4 g/dL Dextran 70). While classical models of shear-induced migration, such as that of Phillips et al. [33], are mainly applied to concentrated suspensions, previous theoretical and experimental studies [34,35] have shown that individual deformable RBCs can also exhibit lateral migration in shear flow due to asymmetric deformation and cell–flow interactions.

2.12. Statistical Analysis

Data are presented as Me (Q1; Q3), where Q1 is the first and Q3 is the third quartile, respectively. The Shapiro–Wilk test was used to evaluate the type of distribution of the data sets. As the results did not confirm normal data distribution in all groups and the variances between the groups were unequal, we used a non-parametric Mann–Whitney test to compare the data of each CLL group with the control group. We considered differences to be significant if $p \leq 0.05$.

Local shear rate profiles were computed using Maple 15 software, Maplesoft [https://www.maplesoft.com], accessed on 5 June 2025.

3. Results

3.1. Clinical and Hematological Characteristics of the CLL Patients and Healthy Controls

The clinical and hematological indices for the CLL patients' groups and the healthy volunteers are presented in Table 2. There were no significant differences in the key hematologic indices between the patient and control groups. However, a lower hemoglobin (Hb) level was observed in the group of patients treated with the combination of Obinutuzumab and Venetoclax. A further analysis revealed some differences within the patient groups themselves. Specifically, lower RBC counts and Ht levels were observed in four patients undergoing Obinutuzumab/Venetoclax treatment, as well as in one untreated patient. Additionally, increased mean corpuscular volume (MCV) and red blood cell distribution width (RDW) values were found in two patients treated with Obinutuzumab/Venetoclax and one untreated patient. Moreover, lower lymphocyte and white blood cell (WBC) counts were detected in five patients in the Obinutuzumab/Venetoclax-treated group. Therefore, although some hematological parameters were altered in some patient groups, the overall differences between patients and healthy controls were minimal.

Table 2. Clinical (age, gender, and Rai stage), and laboratory indices (RBC count; hemoglobin, Hb; hematocrit, Ht; mean corpuscular volume, MCV; mean corpuscular hemoglobin, MCH; mean corpuscular hemoglobin concentration, MCHC; red blood cell distribution width, RDW; total bilirubin; white blood cell, WBC; lymphocytes; platelet count; and fibrinogen) determined for healthy controls and CLL patients. Data are presented as Me (Q1; Q3).

Characteristics	Groups				
	Reference Values	Healthy Controls (n = 16)	CLL Patients Without Treatment (n = 8)	CLL Patients Receiving Obinutuzumab/ Venetoclax (n = 11)	CLL Patients Receiving Ibrutinib (n = 8)
Age (years)	-	58 (45.3; 65.8)	65 (49; 70.8)	72 (64.5; 74.8)	62.5 (54.3; 73.8)
Gender (F/M)		10/6	3/5	5/6	3/5
Rai stage			0	1–4	1–4
RBC count (T/L)	4.60–6.20	4.42 (4.36; 4.59)	5.16 (4.68; 5.26)	4.62 (4.46; 4.82)	4.91 (4.67; 5.09)
Hb (g/L)	140.00–180.00	143.0 (139; 149)	148.5 (141; 160)	140.0 (120; 148) *	141 (138; 147)
Ht (L/L)	0.40–0.54	0.44 (0.41; 0.48)	0.44 (0.42; 0.46)	0.41 (0.37; 0.43)	0.43 (0.41; 0.46)
MCV (fl)	80.00–95.00	89.5 (86.7; 93.0)	87.9 (85.8; 93.8)	88.1 (82.9; 93.6)	89.2 (85.9; 91.0)
MCH (Pg/L)	27.00–32.00	30.1 (29.1; 31.4)	30.3 (28.5; 31.5)	30.1(27.7; 31.3)	29.7 (27.5; 30.2)
MCHC (g/L)	320.00–360.00	345.0 (325.0; 349.5)	339.5 (324; 345)	337.0 (328; 341)	333 (306; 344)
RDW %	11.60–14.80	13.5 (12.6; 14.3)	13.5 (13.2; 15.4)	13.9 (13.3; 14.7)	14.1 (13.5; 14.6)
WBC	3.50–10.50	6.0 (5.5; 6.8)	21.2 (10.1; 71.2) *	3.89 (2.82; 4.20)	6.1 (4.8; 8.1)
Total bilirubin (umol/L)	3.40–20.50	17.4 (8.1; 18.5)	12.0 (8.8; 37.9)	13.0 (9.5; 21.5)	13.4 (11.3; 18.4)
Lymphocytes (ABS)	1.10–3.80	1.84 (1.78; 2.14)	15.8 (5.4; 62.4) *	1.2 (1.0; 1.5)	1.8 (1.1; 3.4)
Platelet count $\times 10^9$/L	142.00–440.00	290.0 (178.0; 337.5)	200 (168; 239)	161 (131; 214)	154 (142; 195)
Fibrinogen (g/L)	1.80–4.50	2.3 (1.98; 2.65)	3.1 (2.3; 3.9)	2.6 (2.4; 2.7)	2.9 (2.7; 3.1)

* Denotes a statistically significant difference ($p < 0.05$) in the laboratory indices between the groups of patients with CLL and the control group.

3.2. Evaluation of Critical Shear Rate for RBC Disaggregation in the Healthy State

An accurate determination of the shear rate of RBC aggregation–disaggregation under experimental conditions is crucial for the precise simulation of microcirculatory conditions and the reliable comparison of healthy and pathological conditions.

In the initial step of our experiments, we aimed to identify the nominal shear rate required to fully disperse RBC aggregates (formed under low-flow conditions) using cells from healthy donors. To achieve this, RBC aggregates formed in the microchannel under the first mode of operation—i.e., at a low shear rate (as outlined in Section 2.7)—were subjected to six progressively increasing shear rates (Table 3). The disaggregation process was examined by assessing the number and size of RBC aggregates, as well as the Aggregate-Area Indicator at high-flow conditions (AAI_H). The latter is a quantitative and reliable parameter for evaluating the aggregation state (described in Section 2.9) at high-flow conditions. The critical minimum shear rate required for disaggregation was determined based on the change in AAI_H in response to the applied shear rates. The experiments were conducted until the shear rate reached a level where the AAI_H no longer exhibited significant changes, indicating that the disaggregation state had stabilized.

Figure 2 shows representative images of RBC aggregates at four selected shear rates (89 s^{-1}, 268 s^{-1}, 446 s^{-1}, and 535 s^{-1}) using a BioFlux microfluidic system and helps visualize the critical shear rate of 446 s^{-1} beyond which RBC disaggregation reaches a plateau.

The extent of RBC disaggregation was accurately determined using Software Image Flow Analysis (described in Section 2.8), which involved assessing the area and number of RBC aggregates not dispersed at the applied shear rates in the obtained images. This software algorithm distinguishes undispersed aggregates based on their size.

Table 3. Aggregation-Area Indicator (AAI_H) and Number (NA_H) at high-flow conditions of undispersed RBC aggregates calculated at six progressively increasing shear rates.

Shear Rate (s^{-1})	NA_H	AAI_H
89	125.7 ± 23.4	0.0524 ± 0.0115
178	87.0 ± 15.6	0.0332 ± 0.0066
268	54.9 ± 9.2	0.0198 ± 0.0043
357	46.3 ± 11.6	0.0158 ± 0.0042
446	17.0 ± 5.7	0.0054 ± 0.0017
535	15.3 ± 1.3	0.0052 ± 0.0006

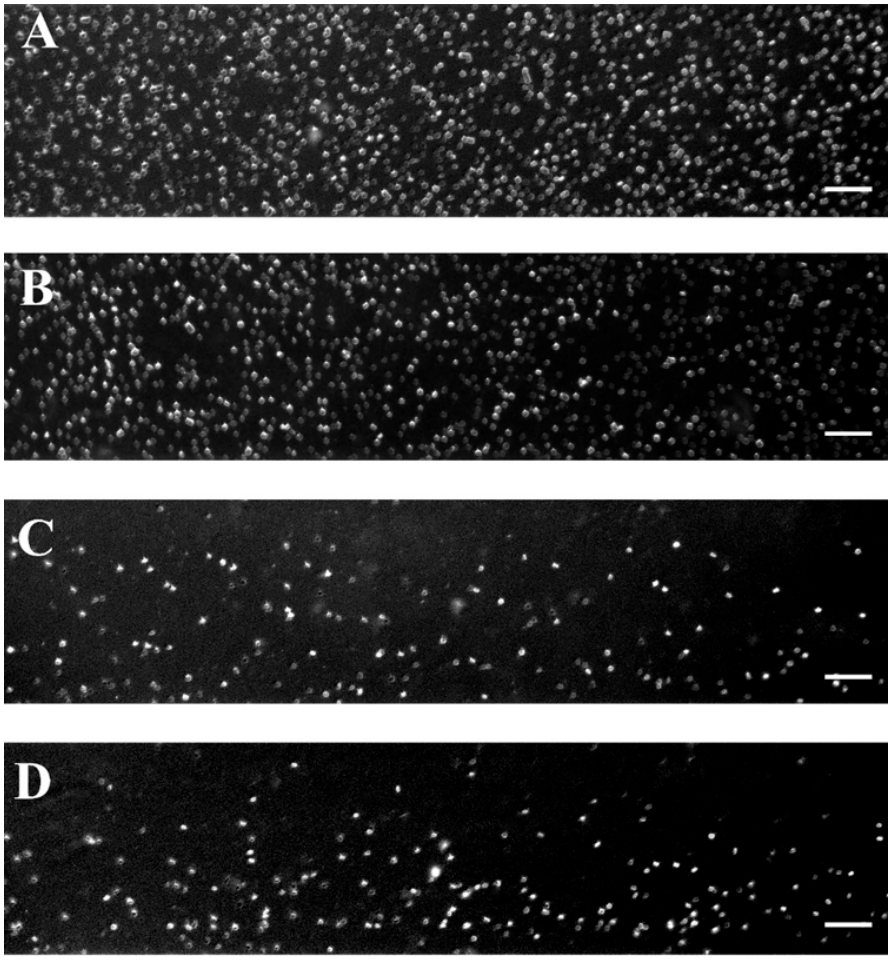


Figure 2. Representative images of RBC aggregates from healthy individuals obtained with the BioFlux microfluidic system under high-flow conditions at (**A**) 89 s^{-1}; (**B**) 268 s^{-1}; (**C**) 446 s^{-1}, and (**D**) 535 s^{-1}. Scale bar—50 μm.

To facilitate interpretation, the visualizations were color-coded to differentiate aggregates by size, particularly at higher shear conditions. In these conditions, populations with smaller aggregate sizes (100–330 μm^2) are more prevalent. This approach enhances the clarity and accuracy of the analysis, especially when examining the effects of varying shear rates on RBC disaggregation.

The color scale applied to the images shown in Figure 2 is further illustrated in Figure 3, providing insight into the size-based classification of RBC aggregates.

As can be seen in Figure 3A, the shear rate of 89 s^{-1} (close to low-flow conditions) is sufficient to destroy the aggregates larger than 1320 μm^2. The image shows relatively large RBC aggregates and rouleaux formations. The aggregates with sizes in the range

of 661–1320 μm^2 were occasionally observed, and their number averaged to 7 ± 2.6. It should be noted that, according to theoretical assumptions, these aggregates tend to migrate toward the center of the visual field of the channel, consistent with the theoretical model described in 3.2.1. The dominant population consisted of Rouleau formations with sizes of 100–330 μm^2 and NA = 119 ± 21 (Figure 3A). The overall Aggregation-Area Index AAI_H had a value of 0.05 ± 0.01 (Table 3). This behavior demonstrated that the applied shear rate cannot disperse all present RBC aggregates.

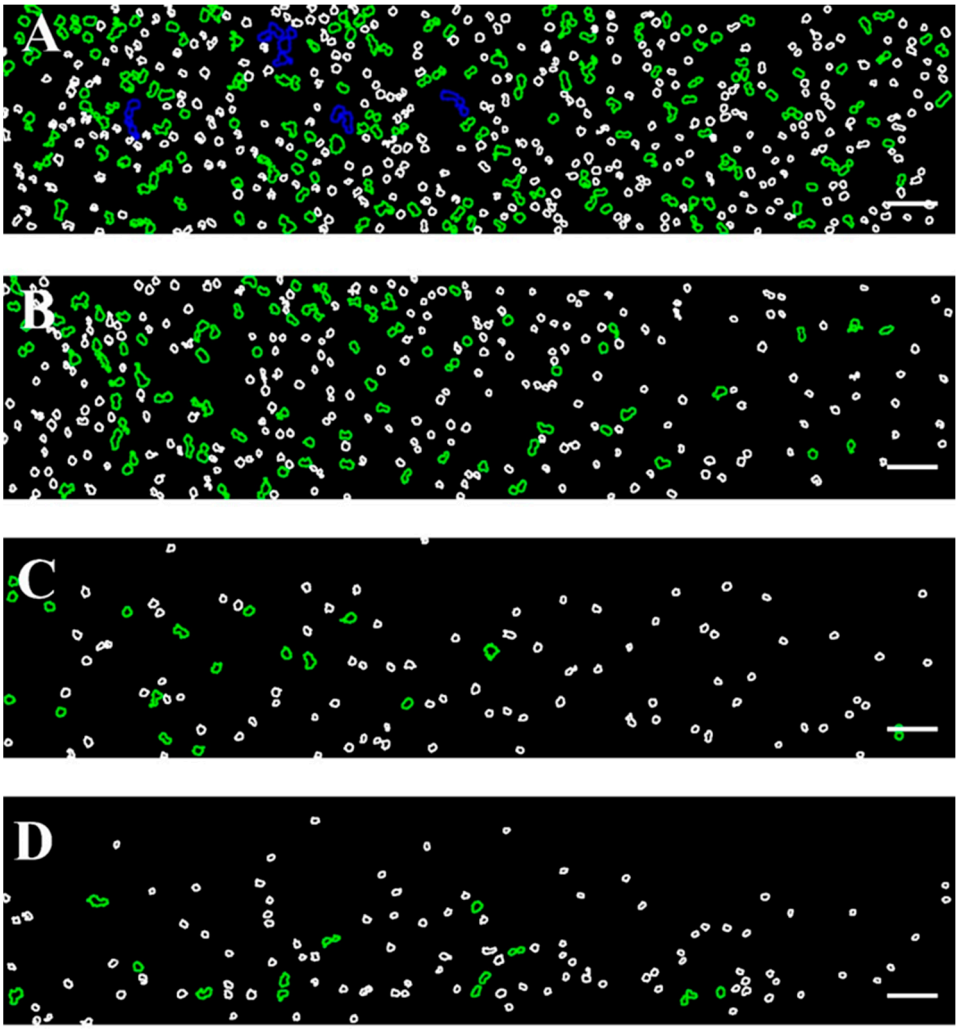


Figure 3. Color-coded representative images of RBCs aggregates from healthy donors, corresponding to those presented in Figure 1, obtained using the BioFlux microfluidic system under high-flow conditions at shear rates of (**A**) 89 s^{-1}, (**B**) 268 s^{-1}, (**C**) 446 s^{-1}, and (**D**) 535 s^{-1}. Aggregated populations are highlighted, enclosed with green (100–330 μm^2) and blue (331–660 μm^2) contours, while individual disaggregated RBCs (area < 99 μm^2) are outlined in white. Scale bar—50 μm.

As the shear rate increases to 268 s^{-1}, the dispersion of RBC aggregates becomes greater because the shear force breaks up the larger aggregates. Despite the increased shear rate, interaction between RBCs was still observed (Figure 3B), with rouleaux being the primary formation. The number of detectable small aggregates was significantly reduced (NA = 54 ± 9), approximately half of that observed at a lower shear rate (i.e., 89 s^{-1}).

At a higher shear rate of 446 s^{-1}, the shear forces were sufficient to disaggregate the majority of RBC aggregates. Fewer rouleaux structures were visible (NA = 17 ± 5.7), and the disaggregated individual RBCs become the dominant population (Figure 3C). Beyond the shear rate of 446 s^{-1}, the observed changes in RBC disaggregation were minimal and

not statistically significant (a shear rate of 535 s^{-1} resulted in NA = 15.3 ± 1.2 (Figure 3D), indicating that the applied shear forces were sufficient to break up the aggregates completely). The AAI_H for the shear rates of 446 s^{-1} and 535 s^{-1} was found to be 0.0054 ± 0.0017 and 0.0052 ± 0.0006, respectively (Table 3).

The NA of the undispersed RBC aggregates and AAI_H values calculated for the selected shear rates are presented in Table 2 and graphically illustrated in Figure 4.

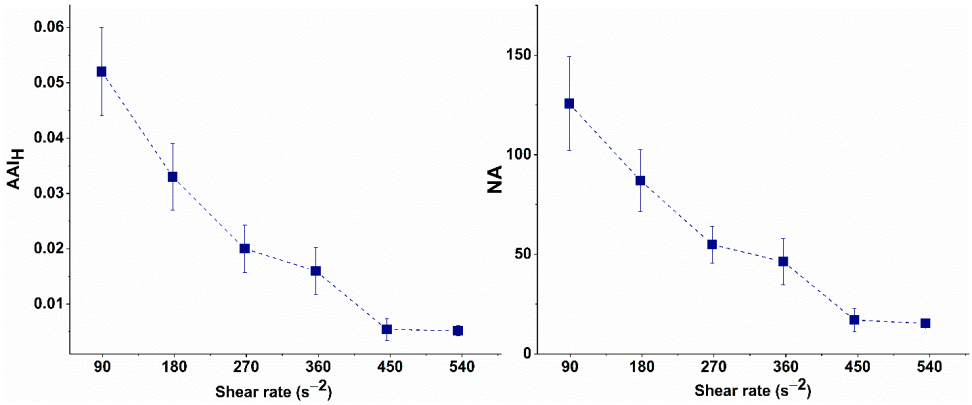


Figure 4. Aggregation-Area Indicator (AAI_H) and Number of Undispersed RBC Aggregates (NA_H) at high-flow conditions of undispersed RBC aggregates as a function of the shear rate.

As shown in Figure 4, the AAI_H gradually decreases as the shear rate increases, reaching its minimum value at 446 s^{-1}. Further increases in shear rate did not result in any significant changes in AAI_H, indicating that most RBC aggregates were dispersed. Similarly, at 446 s^{-1}, the number of undispersed aggregates reached its lowest value, aligning with the plateau in AAI_H.

Therefore, the shear rate of 446 s^{-1} was considered to be the critical shear rate at which RBCs are dispersed, as the observed changes in AAI_H or the number of undispersed aggregates after this point are negligibly small. This shear rate can, therefore, be used in experimental simulations of flow conditions in small blood vessels. It will be applied in subsequent experiments to investigate the behavior of aggregates in patients with CLL and to evaluate the efficacy of treatment.

The local shear rate profiles corresponding to nominal shear rates of 89 s^{-1}, 178 s^{-1}, 268 s^{-1}, 357 s^{-1}, 446 s^{-1}, and 535 s^{-1}, calculated using Equations (1)–(6), are presented in Figure 5. From the plots in Figure 5, we determined the numerical ranges of local shear rates at positions between 25 and 37 μm from the microchannel centerline for each nominal shear rate. This selected region, spanning 25 to 37 μm, corresponds to the approximately 10- to 15-micrometer-thick zone above the bottom surface of the channel, as defined by the BioFlux system, where RBC aggregation and disaggregation are mostly observed. The numerical intervals of local shear rates within this region along the horizontal axis for each nominal shear rate are summarized in Table 4.

Based on the numerical intervals of the local shear rates determined above, we next correlate these values with the sizes of the observed RBC aggregates, as depicted in Figure 3. At local shear rates within the range of 59.33 s^{-1} to 83.25 s^{-1}, both individual RBCs and aggregates with areas ranging from 100 to 330 μm^2 and 331 to 660 μm^2 are observed (Figure 3A). When the local shear rate increases to the range of 178.00 s^{-1} to 249.75 s^{-1} (Figure 3B), RBC aggregates in the 331–660 μm^2 range are no longer present, and the frequency of aggregates in the 100–330 μm^2 range is reduced. At shear rates exceeding 296.67 s^{-1} to 416.25 s^{-1} (Figure 3C,D), RBC aggregates in the 100–330 μm^2 range are rarely observed.

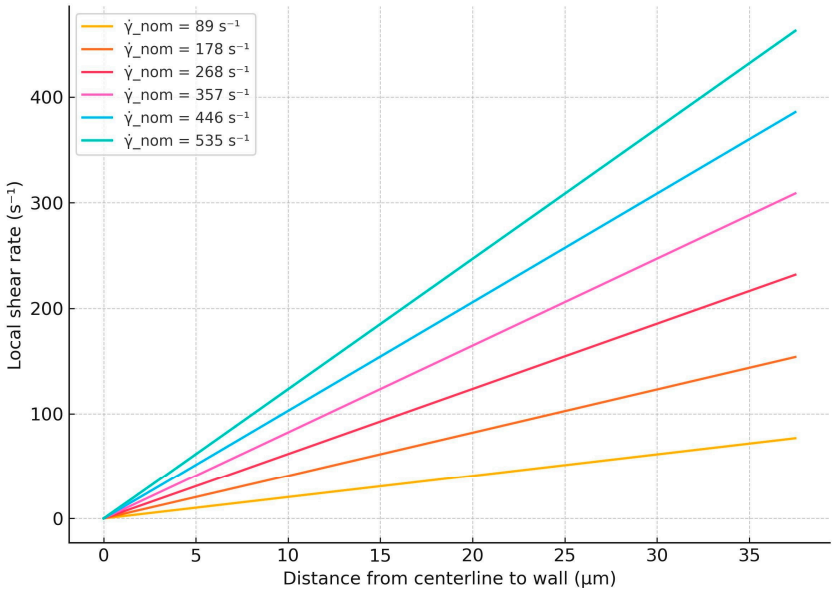


Figure 5. Calculated local shear rate profiles across channel half-height for various nominal shear rates.

Table 4. Numerical ranges of local shear rates at positions between 25 and 37 μm from the microchannel centerline.

Nominal Shear Rate (s^{-1})	Local Shear Rate at 25 μm (s^{-1})	Local Shear Rate at 37 μm (s^{-1})
89	59.33	83.25
178	118.67	166.50
268	178.00	249.75
357	237.33	333.00
446	296.67	416.25
535	356.00	499.50

3.3. RBC Disaggregation and Rheological Indices in CLL Patient Groups and Healthy Individuals

The degree of RBC dispersion is influenced by the previously formed rouleaux and 3D aggregates under low-flow conditions, as well as the intrinsic characteristics of the cells. These factors have important implications for understanding the dynamics of RBC aggregation, particularly in diseases such as CLL, where an altered blood rheology may play a role. To investigate this, we first explore RBC aggregation at a low shear rate (8.9 s^{-1}) (Figures 6 and S1). In the healthy control group, aggregation was minimal and consisted mainly of rouleaux and branched rouleaux formations (Figures S1A and 6A). In contrast, the Software Image Flow Analysis revealed a marked increase in aggregation among CLL samples, where larger RBC aggregates and complex 3D clusters were the predominant populations (Figures 6B and S1B)—structures that were absent in the controls. A similar aggregation pattern was observed in RBC suspensions from CLL patients treated with Obinutuzumab/Venetoclax, suggesting that this treatment does not fully reverse the altered aggregation (Figures 6C and S1C). In contrast, Ibrutinib-treated patients exhibited reduced aggregation, approaching those observed in the healthy control group (Figures 6D and S1D). These findings were detailed and commented on in our previous work investigating the effect of the disease state and therapeutic intervention on RBC aggregation under low-shear conditions in CLL patients [25]. However, it should be noted that the total Aggregation-Area Indicator under a low shear rate (AAI_L) was significantly elevated across all CLL groups compared to the controls (Table 5). The number of aggregates (NA_L) in those

conditions decreased by approximately 30% in untreated CLL and those treated with Obinutuzumab/Venetoclax (Table 5). This reduction in aggregate count is attributed to the formation of larger, more complex 3D networks and cell clusters, which merge individual aggregates into fewer, but substantially larger, structures (Figures 6B–C and S1B,C).

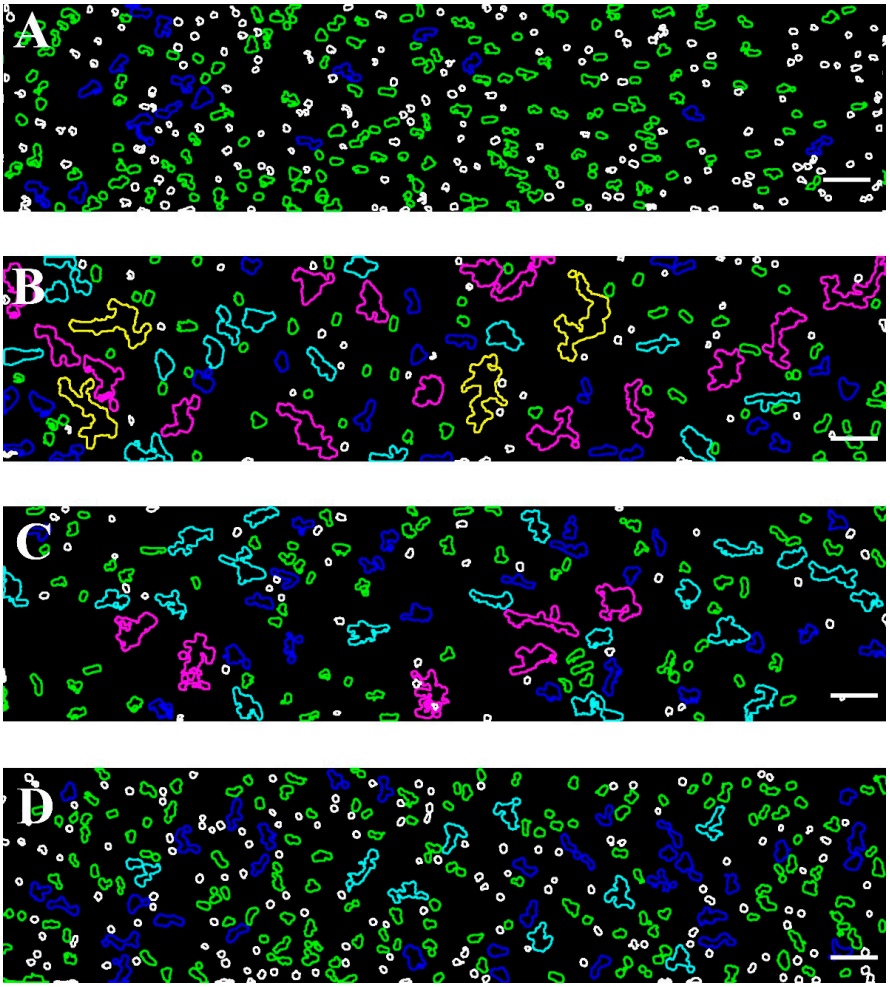


Figure 6. Color-representative images of RBC aggregates, corresponding to the samples shown in Figure S1. The images were acquired using the BioFlux microfluidic system under low-flow conditions (shear rate of 8.9 s^{-1}), from the following: (**A**) healthy individuals; (**B**) patients with CLL not requiring treatment; (**C**) CLL patients treated with Obinutuzumab/Venetoclax; and (**D**) CLL patients treated with Ibrutinib. RBC aggregate populations are presented with color-coded contours based on their projected area: green (100–330 μm^2), blue (331–660 μm^2), light blue (661–1320 μm^2), purple (1321–2700 μm^2), and yellow (>2701 μm^2). Unaggregated individual RBCs (area < 99 μm^2) are presented with white contour. Scale bar—50 μm.

We examined the behavior of RBCs under a high shear rate (446 s^{-1}), simulating the hemodynamic environment within narrow vessels. Using Software Image Flow Analysis, we assessed the proportion of RBC aggregates that remained intact despite the exposure to a high shear flow (Figure 7). In the healthy control group, only a small number (<13) of aggregates, formed by a few numbers of cells, were observed to remain without breaking up under high-shear conditions (Table 5, Figure 7A). These aggregates were readily dispersed under flow, as expected in physiologically normal conditions.

Table 5. Aggregation-Area Indicator (AAI) and Number of RBC Aggregates (NA), at low- (AAI_L, NA_L) and high-shear-rate (AAI_H, NA_H) conditions. Data are presented as Me (Q1; Q3) for the control healthy group, untreated CLL patients, patients treated with Obinutuzumab/Venetoclax, and patients treated with Ibrutinib.

Groups	Low Shear Rate		High Shear Rate	
	AAI_L	NA_L	AAI_H	NA_H
Controls	0.11 (0.09; 0.12)	168 (132; 183)	0.003 (0.002; 0.004)	11.5 (9.5; 14.0)
Untreated CLL	0.14 (0.13; 0.16) *	92.0 (74.3; 147.8) *	0.007 (0.004; 0.011) *	23.0 (19.7; 24.2) *
Obinutuzumab/ Venetoclax	0.13 (0.07; 0.15) *	104 (73; 138) *	0.006 (0.005; 0.007) *	18 (15; 21) *
Ibrutinib	0.15 (0.13; 0.16) *	173 (161; 194)	0.006 (0.004; 0.007) * (n = 5)/ 0.020–0.22 * (n = 3)	17 (14; 21) (n = 5)/ 19–22 * (n = 3)

* Indicates a statistically significant difference ($p < 0.05$) in the values of aggregation indices for CLL patient groups compared to healthy controls.

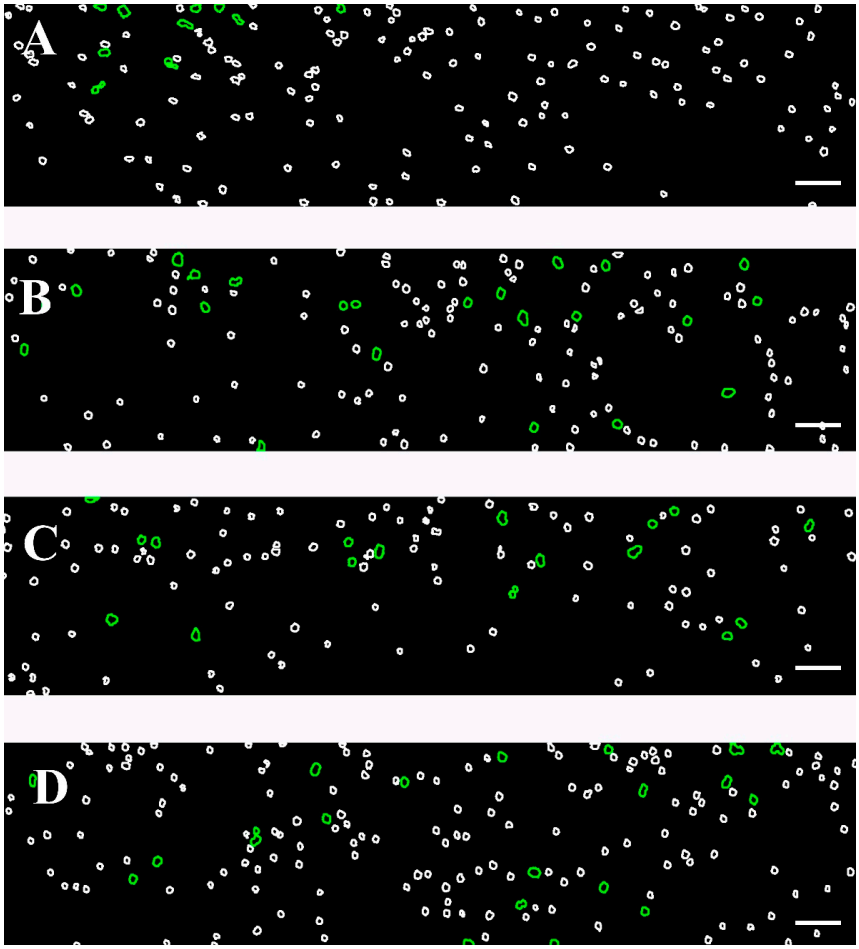


Figure 7. Color-coded representative images of RBC aggregates, presented in Figure S2, based on the developed Software Image Flow Analysis. Images were acquired using the BioFlux microfluidic system under high-flow conditions (after a flow rate of 446 s^{-1}). Images are shown for the following: (**A**) healthy individuals; (**B**) patients with CLL not requiring treatment; (**C**) CLL patients receiving Obinutuzumab/Venetoclax; and (**D**) CLL patients treated with Ibrutinib. RBC aggregated populations are outlined in green (100–330 μm^2), while individual unaggregated RBCs (area < 99 μm^2) are presented with white contours. Scale bar—50 μm.

In the untreated CLL group, the number of RBC aggregates that remained intact under high-shear conditions was approximately twice as high as those observed in the control

group under the same experimental settings (Figure 7B). Correspondingly, the AAI_H also exhibited higher values compared to the control one (p = 0.05; Table 5), indicating an increased aggregate stability and resistance to shear-induced dispersion in CLL.

In the case of the two treated groups, patients receiving Obinutuzumab/Venetoclax and those on Ibrutinib, the number of RBC aggregates that remained intact under high-shear conditions was lower than in the untreated CLL group but still elevated compared to healthy controls (Figure 7C,D, Table 5). The AAI_H was significantly higher in both treated groups compared to controls. However, a notable heterogeneity was observed within the Ibrutinib-treated group. Specifically, for five, the AAI_H values were comparable to those seen in the Obinutuzumab/Venetoclax-treated group, while, in other cases, the AAI_H values were the highest across all study groups. Importantly, although the number of undispersed aggregates in these five cases was close to that of the Obinutuzumab/Venetoclax-treated group, it did not differ statistically from the control group ($p > 0.05$). In contrast, the NA_H of the remaining cases was similar to the untreated group, showing a significant increase relative to controls (p = 0.001) (Table 5).

In addition, a relationship can be established between the areas of the aggregates and the local shear rates based on the calculated intervals presented in Table 4. At local shear rates exceeding the range of 296.67 s^{-1} to 416.25 s^{-1}, in Figure 7A–D, individual RBCs and RBC aggregates with an area of 100–330 μm^2 are observed. These smaller aggregates are more prominent in samples from patients with CLL, including both untreated individuals and those treated with the Obinutuzumab/Venetoclax regimen.

Due to insufficient information, an accurate and generalized assessment of the relationship between local shear rates in the wall and the area of RBC aggregates cannot be made. However, with some conditionality, we can state that, with increasing local shear rates in the microchannel wall, the areas of RBC aggregates decrease.

4. Discussion

RBC aggregation–disaggregation is a key phenomenon affecting blood flow, particularly in microvascular systems, where RBCs are subjected to varying shear rates. The shear flow influences the behavior of RBCs, which, in turn, can affect the overall blood viscosity and oxygen delivery [36]. Under normal physiological conditions, RBCs aggregate in low-shear conditions (<1–10 s^{-1}), and disaggregate under higher shear rates [30]. Estimating the shear rate of erythrocyte dispersion is essential for experimental research and clinical applications. Understanding how RBCs behave at different shear rates can help model the effects of various pathologies on blood flow and oxygen transport.

In this work, we determined the critical shear rate at which almost complete disaggregation occurs in RBC suspensions from control subjects, allowing for a further assessment of the deviations in rheological parameters associated with CLL disease. Thus, determining the main indices of RBC aggregation would help to clarify the changes in the blood rheology of CLL compared to healthy conditions.

A key point to clarify is that the microfluidic system employed in this study uses rectangular microchannels to approximate the conditions of narrow blood vessels. This geometrical approximation has important implications for flow characterization. Notably, despite the application of high nominal shear rates in our experiments, RBC aggregates were consistently observed within the rectangular microchannels. As described in Section 2.11, this observation can be attributed to the non-uniform shear rate distribution inherent to laminar flow in rectangular geometries.

While this study involves certain modeling assumptions, the primary objective remains to assess and compare the extent of residual RBC aggregation between CLL patients and healthy controls at high-flow conditions.

The dispersion of RBC aggregates depends on several factors, including the size of aggregates formed under low-flow conditions, the applied shear rate, and the intrinsic properties of the RBCs themselves. The process of the aggregation of RBCs is an important prerequisite for the subsequent dispersion that occurs in small vessels. Our recent work has demonstrated that the rheological behavior of RBCs from untreated CLL patients significantly differs from that of healthy controls [25]. Specifically, CLL samples exhibited increased cell aggregation and the formation of large three-dimensional aggregates, which were absent in healthy controls. The present findings revealed that RBC aggregation in healthy individuals is reversible under a low shear rate and effectively disperses at higher flow conditions (446 s^{-1}). This reversible behavior enables RBCs to adapt to varying hemodynamic conditions within the bloodstream. In contrast, in CLL patients, more persistent aggregation was observed even at higher shear rates, indicating a disruption in the normal behavior of RBCs. The impaired process of aggregation–disaggregation is likely linked to the reduced cell deformability and/or morphological alterations in the RBCs.

Other factors contributing to this abnormal behavior include the size of the RBC aggregates and the viscosity of the surrounding medium. Since all experiments were conducted under the same controlled conditions regarding viscosity, the intrinsic properties of RBCs were, therefore, the primary factor contributing to the abnormal cell behavior in CLL cases. The RBC aggregated population (100–330 μm^2) formed at a low shear rate was resistant to disruption at the shear rate of 446 s^{-1}—identified as the critical shear rate for RBC disaggregation in healthy samples. These aggregates likely require even higher shear rates to disperse fully. Moreover, the AAI_H exhibited notably higher values in the CLL untreated group than in the healthy control group. The increase in AAI_H values aligns with the hypothesis that, in its untreated state, CLL leads to the formation of either less deformable or relatively more RBC aggregates, which are more difficult to disperse. These findings suggest significant changes in the structural and mechanical properties of CLL RBCs compared to healthy cells. This is consistent with previous reports showing that several diseases, including various types of leukemia, can significantly alter the rheological properties of RBCs [37].

Although no direct relation was found between CLL and RBC membrane defects, it has been reported that some chronic diseases, particularly those affecting the immune system or inducing inflammation, could impair the membrane of RBCs as they traverse damaged tissues. In this context, endothelial cell damage has been observed in chronic lymphoproliferative diseases, potentially contributing to the altered mechanical behavior of RBCs in CLL [38]. In conditions such as CLL, where the immune system is compromised and inflammation is elevated, RBCs may experience mechanical stress through their passage in abnormal microenvironments. In support of this statement, the work by Yoon et al. demonstrated that the elevated secretion of inflammatory cytokines such as IL-6 alters the CLL microenvironment and is associated with the progression of CLL [39]. Consistent with these findings, other studies have also reported elevated levels of the pro-inflammatory cytokines IL-6 and IL-10 in patients with CLL compared to healthy individuals, further implicating inflammation as a contributing factor to altered RBC function [16,40]. Expanding on this, Uziel et al. further explored the interactions between CLL cells and endothelial cells, showing that exosomes released from CLL cells "educate" endothelial cells to become IL-6-producing cells, thereby reinforcing the pro-inflammatory microenvironment [41]. To gain more insights into RBCs' morphometric and nanomechanical features in CLL patients, we plan to evaluate the cell morphology and plasma membrane elasticity that would be a subject of our future publication.

Both patient groups treated with Obinutuzumab/Venetoclax and Ibrutinib in our study showed almost similar behavior at a high shear rate. However, in the low shear

flow, some differences in terms of the size and the structure of the formed aggregates were established. It was found that the RBC aggregation state in Obinutuzumab/Venetoclax-treated samples did not differ from the untreated one, in contrast to Ibrutinib, where the aggregation state of RBCs was restored to levels seen in healthy controls [25].

Nevertheless, the number of undispersed aggregates under high-shear conditions, although reduced in both treated groups compared to the untreated CLL group, remained higher (Table 5), indicating that the applied treatment had only a partial effect on RBC aggregation dynamics. Although no statistically significant difference was observed between the treated groups and the untreated CLL patients, it is important to note that the AAI_H values for the high shear rate were lower in all patients treated with Obinutuzumab/Venetoclax and in 63% of those treated with Ibrutinib. Conversely, higher AAI_H values were observed in the remaining Ibrutinib-treated cases (Table 5), suggesting a potential treatment-dependent RBC disaggregation. Despite these observed trends, AAI_H values in both treated groups remained statistically distinct from healthy controls. This finding suggests that, while treatments, particularly Ibrutinib, may affect the RBC aggregation behavior, they do not fully restore disaggregation to normal levels. This result indicates that, even with treatment, some abnormality in the dispersion of RBC aggregates may still exist. This may indicate the presence of a persistent disease-related change in the mechanical and morphological properties of cells or reflect a mechanism by which these treatments, despite their efficacy in other areas, do not fully normalize aggregate dynamics.

The considerable heterogeneity observed within the Ibrutinib-treated group may suggest that the therapeutic response to Ibrutinib may vary among patients. Some patients may show improvements in disaggregation behavior comparable to those seen with Obinutuzumab/Venetoclax therapy, while others may exhibit less pronounced effects in disaggregation patterns. Overall, these findings emphasize that, while treatments such as Obinutuzumab/Venetoclax and Ibrutinib may ameliorate certain aspects of the disease, they do not fully normalize the process of aggregation–disaggregation dynamics and may exhibit variability in their effectiveness among individual patients. The individual variability of undispersed aggregates and elevated AAI_H values, particularly in a subset of Ibrutinib-treated patients, warrants further investigation to determine whether these patterns correlate with long-term clinical outcomes such as disease progression or the therapeutic response.

5. Conclusions

This study underscores the role of RBC aggregation–disaggregation dynamics as a contributing factor to the rheological disturbances observed in CLL, with potential implications for microvascular function.

The determination of critical shear rates and AAI_H values provided a quantitative assessment of RBC behavior in CLL, allowing for comparisons between healthy individuals, untreated patients, and those receiving targeted therapies. While treatments with Obinutuzumab/Venetoclax and Ibrutinib reduced the number of undispersed aggregates, neither therapy fully normalized RBC disaggregation behavior to the levels observed in healthy controls. Notably, Ibrutinib-treated patients exhibited considerable individual variability, which suggests differential therapeutic impacts on the RBC rheology.

These findings suggest that CLL-associated changes in RBC aggregation–disaggregation behavior are not entirely reversible with the current therapies. The altered RBC dynamics, particularly in the form of elevated AAI_H values, may represent a residual marker of disease activity or a reflection of long-term pathophysiological changes in RBCs. Further investigation is warranted in order to assess the clinical significance of these rheological

abnormalities, their correlation with disease progression, and their potential as therapeutic or prognostic biomarkers.

Supplementary Materials: The following supporting information can be downloaded at: https://www.mdpi.com/article/10.3390/fluids10070167/s1, Figure S1: Representative images of RBC aggregates obtained using the BioFlux microfluidic system under low-flow conditions (after the flow of 8.9 s^{-1}); Figure S2: Representative images of RBC aggregates obtained with the BioFlux microfluidic system under high-flow conditions (after the flow of 446 s^{-1}).

Author Contributions: Conceptualization, S.T.; methodology, A.A.-W., E.V.N., E.A. and T.T.; software, E.A. and T.T.; sample collection, L.G. and M.G.; clinical data, L.G. and M.G.; RBC preparation, M.I., A.A.-W. and A.L.; microfluidic experiments, A.A.-W., M.I. and A.L.; validation, A.A.-W., S.K. and S.T.; formal analysis, S.T., M.I., A.A.-W. and A.L.; investigation, A.A.-W., M.I. and A.L.; writing—original draft preparation, S.T.; writing—review and editing, A.A.-W., S.K., E.V.N., L.G., M.G. and S.T.; supervision, S.T.; funding acquisition, S.T. All authors have read and agreed to the published version of the manuscript.

Funding: This work is supported by Grant KP-06-H73/3, Competition for financial support for basic research projects—2023, Bulgarian National Science Fund.

Data Availability Statement: All data are contained within the manuscript and available upon request.

Acknowledgments: This work is supported by the Competence Center for Mechatronics and Clean Technologies—MIRACle, developed by the Operational Program "Science and Education for Smart Growth" (2014–2020) and the Program "Research, Innovation and Digitalization for Smart Transformation" 2021–2027 (PRIDST), co-financed by the European Union through the European Structural and Investment Funds. We thank Svetoslav E. Anachkov, Department of Chemical and Pharmaceutical Engineering Faculty of Chemistry and Pharmacy, Sofia University, for his assistance with the viscosity measurements.

Conflicts of Interest: The authors declare no conflicts of interest.

Abbreviations

The following abbreviations are used in this manuscript:

RBCs	red blood cells
CLL	Chronic Lymphocytic Leukemia
BCR	B-cell receptor
IL-6	interleukin-6
TNF-α	tumor necrosis factor-alpha
AIHA	autoimmune hemolytic anemia
AAI	Aggregate-Area Indicator
NA	Number of Aggregates
AAI_L	Aggregate-Area Indicator at low-flow conditions
AAI_H	Aggregate-Area Indicator at high-flow conditions
Hb	hemoglobin

References

1. Diez-Silva, M.; Dao, M.; Han, J.; Lim, C.T.; Suresh, S. Shape and Biomechanical Characteristics of Human Red Blood Cells in Health and Disease. *MRS Bull.* **2010**, *35*, 382–388. [CrossRef] [PubMed]
2. Baskurt, O.K.; Meiselman, H.J. Erythrocyte aggregation: Basic aspects and clinical importance. *Clin. Hemorheol. Microcirc.* **2013**, *53*, 23–37. [CrossRef] [PubMed]
3. Mehri, R.; Mavriplis, C.; Fenech, M. Red blood cell aggregates and their effect on non-Newtonian blood viscosity at low hematocrit in a two-fluid low shear rate microfluidic system. *PLoS ONE* **2018**, *13*, e0199911. [CrossRef] [PubMed]
4. Jin, X.; Zhang, Y.; Wang, D.; Zhang, X.; Li, Y.; Wang, D.; Liang, Y.; Wang, J.; Zheng, L.; Song, H.; et al. Metabolite and protein shifts in mature erythrocyte under hypoxia. *iScience* **2024**, *27*, 109315. [CrossRef]

5. Semenov, A.N.; Lugovtsov, A.E.; Shirshin, E.A.; Yakimov, B.P.; Ermolinskiy, P.B.; Bikmulina, P.Y.; Kudryavtsev, D.S.; Timashev, P.S.; Muravyov, A.V.; Wagner, C.; et al. Assessment of Fibrinogen Macromolecules Interaction with Red Blood Cells Membrane by Means of Laser Aggregometry, Flow Cytometry, and Optical Tweezers Combined with Microfluidics. *Biomolecules* **2020**, *10*, 1448. [CrossRef]
6. Nader, E.; Skinner, S.; Romana, M.; Fort, R.; Lemonne, N.; Guillot, N.; Gauthier, A.; Antoine-Jonville, S.; Renoux, C.; Hardy-Dessources, M.D.; et al. Blood Rheology: Key Parameters, Impact on Blood Flow, Role in Sickle Cell Disease and Effects of Exercise . *Front. Physiol.* **2019**, *10*, 1329. [CrossRef]
7. Lee, K.; Kinnunen, M.; Khokhlova, M.D.; Lyubin, E.V.; Priezzhev, A.V.; Meglinski, I.; Fedyanin, A.A. Optical tweezers study of red blood cell aggregation and disaggregation in plasma and protein solutions. *J. Biomed. Opt.* **2016**, *21*, 35001. [CrossRef]
8. Brenner, B.; Koren, A.; Engelberg, S.; Notti, I.; Tatarsky, I. Increased red blood cell aggregability as a contributory factor for vascular occlusion in sickle cell disease. *Am. J. Hematol.* **1992**, *39*, 176–179.
9. Chung, S.M.; Oh, J.H.; Moon, J.S. Critical Shear Stress is Associated with Diabetic Kidney Disease in Patients with Type 2 Diabetes. *Sci. Rep.* **2018**, *8*, 908. [CrossRef]
10. Nader, E.; Nougier, C.; Boisson, C. Increased blood viscosity and red blood cell aggregation in patients with COVID-19. *Am. J. Hematol.* **2022**, *97*, 283–292. [CrossRef]
11. Le Devehat, C.; Vimeux, M.; Bondoux, G.; Bertrand, A. Red blood cell aggregation and disaggregation in diabetes mellitus. *Clin. Hemorheol.* **1989**, *9*, 845–854. [CrossRef]
12. Razavian, S.M.; Del Pino, M.; Simon, A.; Levenson, J. Increase in erythrocyte disaggregation shear stress in hypertension. *Hypertension* **1992**, *20*, 247–252. [CrossRef] [PubMed]
13. Caligaris-Cappio, F. Inflammation, the microenvironment and chronic lymphocytic leukemia. *Haematologica* **2011**, *96*, 353–355. [CrossRef] [PubMed]
14. Hallek, M.; Al-Sawaf, O. Chronic lymphocytic leukemia: 2022 update on diagnostic and therapeutic procedures. *Am. J. Hematol.* **2021**, *96*, 1679–1705. [CrossRef]
15. Saluja, S.; Bansal, I.; Bhardwaj, R.; Beg, M.S.; Palanichamy, J.K. Inflammation as a driver of hematological malignancies. *Front. Oncol.* **2024**, *14*, 1347402. [CrossRef] [PubMed]
16. Fayad, L.; Keating, M.J.; Reuben, J.M.; O'Brien, S.; Lee, B.N.; Lerner, S. Interleukin-6 and interleukin-10 levels in chronic lymphocytic leukemia: Correlation with phenotypic characteristics and outcome. *Blood* **2001**, *97*, 256–263. [CrossRef]
17. Rozovski, U.; Keating, M.J.; Estrov, Z. Targeting inflammatory pathways in chronic lymphocytic leukemia. *Crit. Rev. Oncol. Hematol.* **2013**, *88*, 655–666. [CrossRef]
18. Hamblin, T.J. Autoimmune complications of chronic lymphocytic leukemia. *Semin Oncol.* **2006**, *33*, 230–239. [CrossRef]
19. Barcellini, W. New insights in autoimmune hemolytic anemia: From pathogenesis to therapy. *Int. J. Lab. Hematol.* **2015**, *37* (Suppl. S1), 1–10. [CrossRef]
20. Reed, J.C.; Pellecchia, M. Apoptosis-based therapies for hematologic malignancies. *Blood* **2005**, *106*, 408–418. [CrossRef]
21. Parmar, S.; Patel, K.; Pinilla-Ibarz, J. Ibrutinib (imbruvica): A novel targeted therapy for chronic lymphocytic leukemia. *Pharm. Ther.* **2014**, *39*, 483–519.
22. Soto, F.; Martinez, D.F.; Del Castillo, L. Microfluidic technologies in blood rheology and red blood cell mechanics. *Microfluid. Nanofluidics* **2017**, *21*, 121.
23. Ganesan, M.; Kappanayil, M.; Suresh, S. Microfluidic models for sickle cell disease and other hemorheological disorders. *J. Hematol.* **2019**, *9*, 53–64.
24. Alexandrova-Watanabe, A.; Abadjieva, E.; Giosheva, I.; Langari, A.; Tiankov, T.; Gartchev, E.; Komsa-Penkova, R.; Todinova, S. Assessment of Red Blood Cell Aggregation in Preeclampsia by Microfluidic Image Flow Analysis—Impact of Oxidative Stress on Disease Severity. *Int. J. Mol. Sci.* **2024**, *25*, 3732. [CrossRef] [PubMed]
25. Alexandrova-Watanabe, A.; Abadjieva, E.; Gartcheva, L.; Langari, A.; Ivanova, M.; Guenova, M.; Tiankov, T.; Strijkova, V.; Krumova, S.; Todinova, S. The Impact of Targeted Therapies on Red Blood Cell Aggregation in Patients with Chronic Lymphocytic Leukemia Evaluated Using Software Image Flow Analysis. *Micromachines* **2025**, *16*, 95. [CrossRef]
26. Hallek, M.; Cheson, B.D.; Catovsky, D.; Caligaris-Cappio, F.; Dighiero, G.; Döhner, H.; Hillmen, P.; Keating, M.; Montserrat, E.; Chiorazzi, N. iwCLL guidelines for diagnosis, indications for treatment, response assessment, and supportive management of CLL. *Blood* **2018**, *131*, 2745–2760. [CrossRef] [PubMed]
27. Hallek, M.; Cheson, B.D.; Catovsky, D.; Caligaris-Cappio, F.; Dighiero, G.; Döhner, H.; Hillmen, P.; Keating, M.J.; Montserrat, E.; Rai, K.R. International Workshop on Chronic Lymphocytic Leukemia. Guidelines for the diagnosis and treatment of chronic lymphocytic leukemia: A report from the International Workshop on Chronic Lymphocytic Leukemia updating the National Cancer Institute-Working Group 1996 guidelines. *Blood* **2008**, *111*, 5446–5456. [PubMed]
28. Pribush, D.A.; Zilberman-Kravits, N.; Meyerstein, N. The mechanism of the dextran-induced red blood cell aggregation. *Eur. Biophys. J.* **2007**, *36*, 85–94.

29. Neu, B.; Meiselman, H.J. Depletion-mediated red blood cell aggregation in polymer solutions. *Biophys. J.* **2002**, *83*, 2482–2490. [CrossRef]
30. Baskurt, O.K.; Meiselman, H.J. Blood rheology and hemodynamics. *Semin Thromb Hemost.* **2003**, *29*, 435–450. [CrossRef]
31. Clavería, V.; Aouane, O.; Thiébaud, M.; Abkarian, M.; Coupier, G.; Misbah, C.; Johna, T.; Wagner, C. Clusters of red blood cells in microcapillary flow: Hydrodynamic versus macromolecule-induced interaction. *Soft Matter.* **2016**, *12*, 8235–8245. [CrossRef] [PubMed]
32. Kim, H.; Zhbanov, A.; Yang, S. Microfluidic Systems for Blood and Blood Cell Characterization. *Biosensors* **2023**, *13*, 13. [CrossRef] [PubMed]
33. Phillips, R.J.; Armstrong, R.C.; Brown, R.A. A constitutive equation for concentrated suspensions that accounts for shear-induced particle migration. *Phys. Fluids A* **1992**, *4*, 30–40. [CrossRef]
34. Abkarian, M.; Faivre, M.; Viallat, A. Swinging of red blood cells under shear flow. *Phys. Rev. Lett.* **2007**, *98*, 188302. [CrossRef] [PubMed]
35. Secomb, T.W. Blood flow in the microcirculation. *Annu. Rev. Fluid Mech.* **2017**, *49*, 443–461. [CrossRef]
36. Neu, B.; Meiselman, H.J. Red blood cell aggregation. In *Handbook of Hemorheology and Hemodynamics*; Baskurt, O.K., Hardeman, M.R., Rampling, M.W., Meiselman, H.J., Eds.; IOS Press: Amsterdam, The Netherlands, 2007; pp. 114–136.
37. Bortolato, S.A.; Canales, M.A.M.; Riquelme, B.D.; Raviola, M.; Leguto, A.J.; Rebechi, J.P.; Ponce de León, P.; Korol, A.M. New insights into the analysis of red blood cells from leukemia and anemia patients: Nonlinear quantifiers, fractal mathematics, and Wavelet Transform. *Phys. A Stat. Mech. Appl.* **2021**, *567*, 125645. [CrossRef]
38. Davydkin, I.L.; Kuzmina, T.P.; Naumova, K.V.; Khayretdinov, R.K.; Danilova, O.E.; Stepanova, T.Y.; Osadchuk, A.M.; Mordvinova, E.V. Endothelial dysfunction in patients with lymphoproliferative disorders and its changes in the course of polychemotherapy. *Russ. Open Med. J.* **2020**, *9*, e0309. [CrossRef]
39. Yoon, J.Y.; Lafarge, S.; Dawe, D.; Lakhi, S.; Kumar, R.; Morales, C. Association of interleukin-6 and interleukin-8 with poor prognosis in elderly patients with chronic lymphocytic leukemia. *Leuk Lymphoma* **2012**, *53*, 1735–1742. [CrossRef]
40. Lai, R.; O'Brien, S.; Maushouri, T.; Rogers, A.; Kantarjian, H.; Keating, M.; Albitar, M. Prognostic value of plasma interleukin-6 levels in patients with chronic lymphocytic leukemia. *Cancer* **2022**, *95*, 1071–1075. [CrossRef]
41. Uziel, O.; Lipshtein, L.; Sarsor, Z.; Beery, E.; Bogen, S.; Lahav, M.; Regev, A.; Kliminski, V.; Sharan, R.; Gervits, A.; et al. Chronic Lymphocytic Leukemia (CLL)-Derived Extracellular Vesicles Educate Endothelial Cells to Become IL-6-Producing, CLL-Supportive Cells. *Biomedicines* **2024**, *12*, 1381. [CrossRef]

Disclaimer/Publisher's Note: The statements, opinions and data contained in all publications are solely those of the individual author(s) and contributor(s) and not of MDPI and/or the editor(s). MDPI and/or the editor(s) disclaim responsibility for any injury to people or property resulting from any ideas, methods, instructions or products referred to in the content.